Chapter 4

Macro to micro phase separation in a collection of chiral active swimmers

4.1 Introduction

In the previous Chapter 3, we analyse the motion of the active run and tumble particle in the presence of passive particle. Where we found motion of the passive particle is always shows subdiffusive, but motion of the active always shows crossover from early time ballistic to late time diffusion. Further we also found that crossover time scale for passive particle increasing with increasing size ratio. As we know active Brownian particles (ABPs) are prominent example of active matter [Ghosh & Fischer (2009); Kumar et al. (2014); Levis & Liebchen (2018); Liao & Klapp (2018); Toner et al. (2005)]. ABP combine Brownian motion with self-propulsion. Motile microorganisms are frequently characterised as ABPs, in addition to artificial self-propelled microparticles [Bechinger et al. (2016); Levis & Liebchen (2018); Liao & Klapp (2018)]. Even bacteria that conduct a run-and-tumble action [Bechinger et al. (2016); Peruani & Bär (2013); Shaebani et al. (2020)] such as Escherichia Coli, have been effectively classified as ABP. One of the remarkable property of ABP's are motility induced phase separation (MIPS) without any

cohesive interaction among the particles [Bechinger et al. (2016); Gonnella et al. (2015); Kumar et al. (2021); Kümmel et al. (2013); Leptos et al. (2009)]. Most of theoretical and simulation study of ABP is focused on systems without chirality [Gonnella et al. (2015)]. But chirality is an inherent property in many natural active particles [Bechinger et al. (2016); Elgeti et al. (2010); Ghosh & Fischer (2009); Kraft et al. (2013); Liao & Klapp (2018); Menzel (2015)]. Hence effect of chirality on the properties of ABPs is an important question to be asked. In [Keaveny & Shelley (2009); Keaveny et al. (2013)] motion of microswimmers is studied in the presence of chirality. Chirality leads to the deviation of particle trajectory from the straight line motion. In a recent review [Löwen (2016)], it is shown that an individual or collection of chiral or circle swimmer can show interesting properties. When present in bulk they can also show active turbulence [Ginelli (2016); Keaveny et al. (2013); Levis & Liebchen (2018); Winkler (2016)]. Our study is motivated with recent study of [Ma & Ni (2022)] dynamic clustering of chiral active particles. Chirality of particles suppress the motility induced phase separation present for nonchiral active Brownian particles [Cates & Tailleur (2015)]. Hence effect of chirality on the properties of individual and collective behaviour of active particles can give good understanding of another class of nonequilibrium system called chiral active particles (CAP). Most of the recent study of CAP have focused on the effect of chirality on the kinetics or steady state properties of active particles on the variation of activity or packing densities of the particles [Ghosh & Fischer (2009); Levis & Liebchen (2018); Liao & Klapp (2018)]. The study of properties of active particles, on the variation of chirality is very scarce. But such study can provide a good understanding of effect of chirality on the properties of active particles. The two extremes: small or large chirality is trivial for the first case we expect the results of ABPs in the collection and for the later case we expect mainly the confined circular motion. But what happen when we slowly tune the chirality from small to large values still unexplored. In the present work we focus on this effect

of variation of chirality on the properties of active particles. Here we show the kinetics and steady state properties of CAPs on the variation of chirality and activity. The system is found in three distinct phases (i) for small chirality, when activity dominates, system shows the enhanced diffusion [Klamser et al. (2018); Ma & Ni (2022); Omar et al. (2021)] and macroscopic clustering as found in MIPS. In the second phase where both activity and chirality are in competition, we find some clustering, but no macro phase separation. For larger chirality, the chirality dominates over activity and dynamics of particles is mostly confined to its location and no clustering is observed. Our article divided in the following sections: In section 4.2, we give the detailed description of our model. In section 4.3 discuss about the results of numerical simulation of the system. In section 4.5 we conclude our result and discussion about the future directions of our study.

4.2 Model

Our system consists of N chiral active particles (CAP) of radius a_0 on a two-dimensional substrate. On the substrate each i^{th} particle is represented by its position vector $\mathbf{r}_i(t)$ and orientation $\theta_i(t)$, at time t. The dynamics of the particle is governed by the overdamped Langevin equation [Ramaswamy (2017); Semwal et al. (2021); Uhlenbeck & Ornstein (1930)]:

$$\partial_t \mathbf{r}_i = v\hat{\mathbf{n}}_\mathbf{i} + \mu_1 \sum_{j\neq i} \mathbf{F}_{ij} \tag{4.1}$$

$$\partial_t \theta_i = \omega + \sqrt{2D_r}\eta_\mathbf{i} \tag{4.2}$$

The first term on the right hand side (RHS) of eqn. 4.1 is due to the activity of the particle, and v is its self-propulsion speed. The particle moves along its unit orientation direction vector $\hat{\mathbf{n}}_i = (\cos\theta_i, \sin\theta_i)$ with speed v. The second term represents the steric force, $\mathbf{F}_{ij} = F_{ij}\hat{\mathbf{r}}_{ij}$, which takes care of the repulsive interaction, acting on the i^{th} particle

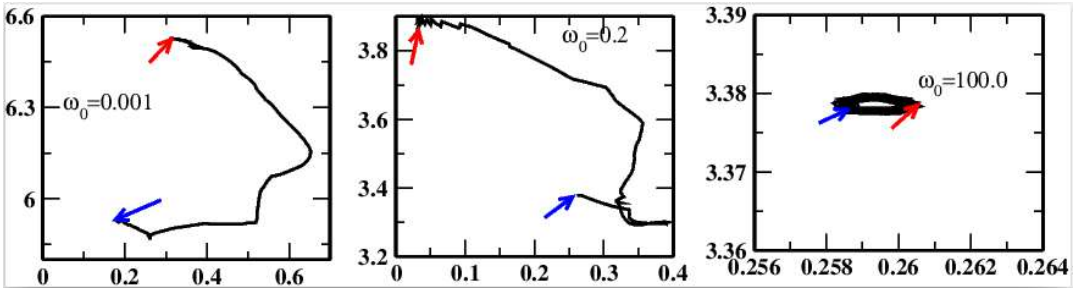

Fig. 4.1 (color online) Trajectory of the particle in trapped state(a), motion of the particle from superdiffusive to diffusive (b), where blue arrow shows the starting point and red arrow shows the end point of trajectory.

due to its neighbouring particles in contact with it. Hence we consider $F_{ij} = k(2a_0 - r_{ij})$ if $r_{ij} \leq 2a_0$ and $F_{ij} = 0$ if $r_{ij} \geq 2a_0$, where r_{ij} is the centre to centre distance between i^{th} and j^{th} particles, $r_{ij} = |\mathbf{r}_i - \mathbf{r}_j|$. k is the strength of the force, F_{ij} is tuned by the mobility μ_1 of the particles. Further, the orientation of the particle is updated by eqn. (4.2) where ω is the chirality (angular velocity) of the particle and η_i is Gaussian white noise term. D_r is the rotational diffusivity. The smallest time step considered is $\Delta t = 0.005$. We define the dimensionless chirality as $\omega_0 = \frac{\omega}{D_r}$, and the dimensionless activity of the particles as $v_0 = \frac{v}{a_0 \times D_r}$. We start our simulation with random position and orientation of particles on the substrate and evolve the system by integrating the eqn. 4.2 and 4.2 using Euler's integration scheme. The system is simulated for total simulation time steps of 10^6. One simulation step is counted after update of all the particles once. All the physical quantities calculated here are averaged 50 realizations. Simulation is performed in box of size $L = 150 \times a_0$, with packing fraction $\frac{N\pi\sigma^2}{L^2} = 0.6$.

4.3 Results

We first observe the trajectory of a single particle in the collection for different chirality. In Fig. 4.1(a-c) we show the trajectory for three different values of chirality $\omega_0 = 0.001$, 0.2 and 100 respectively and for fixed self-propulsion speed $v_0 = 10$. For small $\omega_0 = 0.001$,

Fig. 4.1(a) trajectory looks very extended. The blue and black arrows show the starting and end point of trajectory respectively. For intermediate $\omega_0 = 0.2$, Fig. 4.1(b), trajectory looks localised for early time and then extended towards the end. For large $\omega_0 = 100$, Fig. 4.1(c) trajectory is always confined within a small region. For comparison the time difference from the start and end of the trajectory is kept the same for all three cases.

To quantify the above observation, we measure the mean square displacement of the particles for different chirality. We define the particles mean square displacement as $\Delta(t) =< (r_i(t+t_0) - r_i(t_0))^2 >$ where $< .. >$ denotes average over all the particles, many reference times t_0 and over different realisations. In general the dynamics of active particles shows an early time ballistic dynamics and then crossover to late time diffusion. In Fig. 4.2 we show the behaviour of MSD for fixed activity $v_0 = 10.0$ and varying the chirality. For zero chirality system shows a very clear crossover from early time ballistic to late time diffusion. As we introduce chirality, $\Delta(t)$ shows oscillations, which is due to the oscillations of particles trajectory for finite chirality. The periodic oscillations increases and crossover time decreases on increasing ω_0. We extract the typical crossover time $t_c(\omega_0)$ by fitting the MSD with the persistent random walk= $\Delta(t) = 4D_{eff}t[1 - exp(-t/t_c)]$, for different ω_0 and plot is shown in the inset of Fig. 4.2(a). The crossover time remains almost constant for smaller chirality $\omega_0 \leq 0.1$ and then show a smooth decay for intermediate $0.1 < \omega_0 < 10.0$ and then decays sharply for larger $\omega_0 > 10.0$. For large chirality the dynamics of particle is no longer diffusive for late time and hence t_c cannot be calculated. To further characterise the dynamics of particle we also calculated the late time effective diffusivity $D_{eff}(\omega_0)$ for different ω_0 for three different $v_0 = 1, 10$ and 100. The late time effective diffusivity D_{eff} is obtained by $D_{eff} = \lim_{t\to\infty} \frac{\Delta(t)}{4t}$ The plot of $D_{eff}(\omega_0)$ vs. ω_0 is shown in Fig. 4.2(b). For large activities $v_0 = 10$ and 100, we find that for small chirality $\omega_0 \leq 0.1$, the $D_{eff}(\omega_0)$ remains flat and then for the intermediate $\omega_0 \in (0.1, 10)$, shows a shallow region with slow decay and finally for larger chirality decay sharply to very small

values. For smaller activities $v_0 = 1.0$, the dynamics for larger chirality is mostly confined hence the D_{eff} cannot be defined.

For comparison we also calculated the MSD for noninteracting single chiral particle analytically. The calculation is performed by making the interaction force term zero. In the absence of interaction, the overdamped Langevin eqn. 4.1 and 4.2 reduces to:

$$\partial_t \mathbf{r}_i = v\hat{\mathbf{n}}_\mathbf{i} \tag{4.3}$$

$$\partial_t \theta_i = \omega + \sqrt{2D_r}\eta_\mathbf{i} \tag{4.4}$$

these equations can be solved to obtain the mean square displacement of chiral active particle without interaction. The first and second moments of $\theta(t)$ are simply $<\theta(t)>= \theta_0 + \omega t$ and $<\theta^2(t)>= \omega^2 t^2 + 2D_r t$, where, $\theta_0 = \theta(t=0) = 0$. Using this, the second moment of $r(t)$ or the mean square displacement is obtained:

$$<r^2(t)>= \Delta(t) = \frac{2v^2}{(\omega^2 + D_r^2)^2}[\omega^2 - D_r^2 + D_r(D_r^2 + \omega^2)t + e^{-D_r t}((D_r^2 - \omega^2)cos(\omega t) - 2D_r\omega sin(\omega t))]$$

The late time diffusivity or D_{eff} is defined to be $\lim_{t\to\infty}\frac{\Delta(t)}{4t}$. Hence in the absence of interaction the diffusivity is given by the expression:

$$D_{eff} = \frac{v^2 D_r}{2(\omega^2 + D_r^2)} \tag{4.5}$$

Writing D_{eff} in terms of dimensionless chirality ω_0,

$$D_{eff} = \frac{v_0^2}{2D_r(\omega_0^2 + 1)} \tag{4.6}$$

In Fig. 4.2(b), lines are from the analytical expression of D_{eff} as given in eqn. 4.6. For small chirality for all activities the D_{eff} for noninteracting case is smaller than the interacting full numerical simulation. Later we are going to show for the same range of chirality particles shows the clustering. Hence in this regime collective dynamics of particles is responsible for the enhanced dynamics in comparison to noninteracting single particle dynamics. As we increase chirality, the noninteracting D_{eff} decay smoothly to zero values for all activities, whereas for interacting case, it shows a small plateau for intermediate chirality. Hence we can say that the second region with intermediate chirality is all due to the interaction between the particles. Later we are going to explore the system more for the three different regions for full numerical study of interacting system. Further we classify the three regions for the full interacting system as region *I*, *II* and *III* as marked in Fig. 4.2(b). In next sections we discuss in detail the how does the clustering of particles is changed due to the effectively three different dynamics in the three regions.

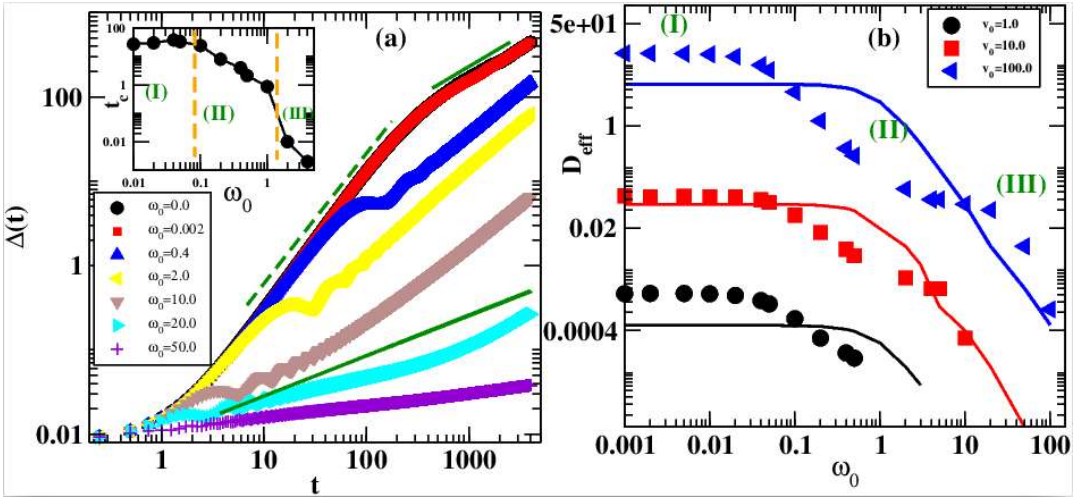

Fig. 4.2 (color online) Plot of MSD, Δ(t) vs. time t for different value of chirality(a) [inset plot crossover time t_c vs. ω_0 for plot (a), dotted orange line shows three different regime MAC,MIC and homogeneous], D_{eff} vs. ω_0 for different value of v_0, different symbol shows numerical data, straight line shows data from analytical eqn. 4.5.

4.3.1 Cluster size distribution

In the previous section we studied the effect of chirality on the effective dynamics of the system. Now we study how the change in effective dynamics changes the clustering and phase behaviour of particles in the system. In Fig. 4.4(a-c) we show the snapshots of particles for three different $\omega_0 = 0.001, 1.0$ and 50 respectively in regions I, II and III for activity $v_0 = 10.0$. For the I region, Fig. 4.4(a) we clearly see the macroscopic clustering in the system, As we approach to the region II, Fig. 4.4(b) we see the microscopic clustering, Finally in region III, Fig. 4.4(c) there is no clustering and system is homogeneously distributed. Further we calculate the cluster size distribution (CSD) for different chirality for activity $v_0 = 10$ as shown in Fig. 4.3(a). The CSD is defined for the particles connected by a most probable distance r_0 in a given configuration. In Fig. 4.3(a) we plot the normalised CSD $P(n)$ vs. n for different chirality ω_0, specifically chosen in the three regions of the D_{eff} plot shown in Fig. 4.2(b). n is the size of the cluster. We find that for small $\omega_0 = 0.2$, $P(n)$ decays as power law $\simeq \frac{1}{n^{-\alpha}}$ for large n, with exponent $\alpha = 2$ as reported in previous studies [Ding & Aidun (2006)]. As we increase ω_0 and system transits into the second phase $P(n)$ still decay as power law, but the exponent $\alpha \simeq 3$, On further increasing the chirality of the particle $P(n)$ decays exponentially with n. Hence the three regions which are defined based on the effective dynamics of particles in the steady state: also lead to different types of clustering of particles. We also calculated the average cluster size $n_{av}(\omega_0)$ for different ω_0 and found that it also shows three different regions as shown in Fig. 4.3(b) for $v_0 = 10$. $n_{av}(\omega_0)$ is defined as $n_{av}(\omega_0) = \int nP(n)dn$. In the first region as shown in Fig. 4.3(b), system shows the formation of macroscopic clusters with an average cluster size $n_{av}(\omega_0)$ around 75 in the (I) phase, $n_{av}(\omega_0)$ varies from 70 to 25 for the ω_0 in the (II) phase. As we further increase ω_0, system enters in to the third region and homogeneous state of the particles and n_{av} decay sharply to very small values. Now we try to understand how the chirality affects the structural ordering of particles in the system.

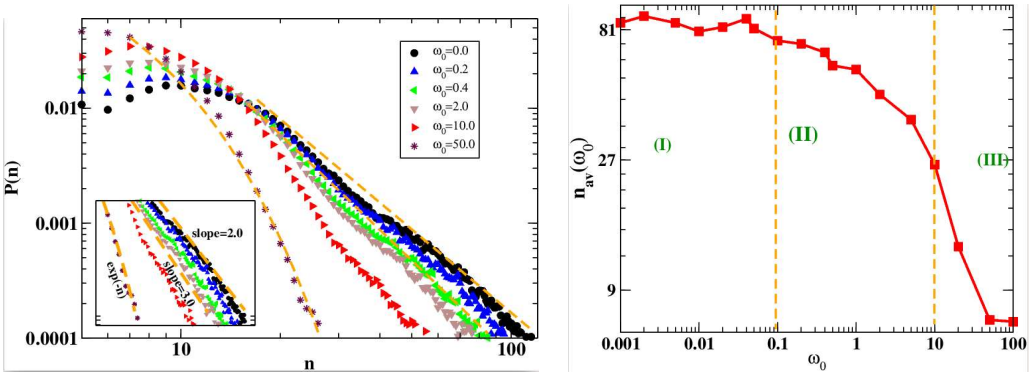

(a) (b)

Fig. 4.3 (a) P(n) vs mean number of particle n for $v_0 = 50$, where orange dotted line is fitting line in different regime(inset plot is zoom plot for fitting line). (b) $n_{av}(\omega_0)$ vs. ω_0 for system size $150 \times a_0$(dotted orange line shows three different regime MAC,MIC and homogeneous phase).

4.3.2 Structural ordering

We further try to understand the effect of chirality on phase separation and structural ordering in the system. We define local density around a particle ρ_{loc} as function of chirality for different activities. In general a nonchiral system shows a motility induced phase separation (MIPS) on tuning the activity or packing fraction [Klamser et al. (2018)]. Here we are interested on the effect of chirality keeping packing fraction fixed and for different activity. We define the local density ρ_{loc} with the help of the number of particles surrounding a given particle. $\rho_{loc} = \frac{n_p}{6}$, where n_p is the number of particles surrounding the given particle. For a perfectly packed surrounding we expect number is 6 for hexagonal close packed (HCP) structure and then we define that the $\rho_{loc} = 1$. Hence in this way for a given snapshot of the system we have a distribution of ρ_{loc}, $P(\rho_{loc})$ where the probability distribution function $P(\rho_{loc})$ is obtained by looking ρ_{loc} of each particle. For a perfect clustered phase the ρ_{loc} will be peaked around 1 for completely homogeneous phase ρ_{loc} will approach the mean packing density $\rho_{loc} = 0.6$ of the system. In Fig. 4.5(a) we show the plot of location of peaks ρ_0 of $P(\rho_{loc})$ vs. ω_0 for three different values of activities $v_0 = 1, 10, 30$. We find that for small $v_0 = 1$, $P(\rho_{loc})$ has only one peak. For small ω_0, ρ_0

remains flat close to 0.7 and then decay to mean packing density 0.6 for larger chirality. For activity $v_0 = 10$, the $P(\rho_{loc})$ is bimodal (data not shown) and location of two peaks at smaller and larger ρ_0's is shown in Fig. 4.5(a). For small chirality or in the I region the two peaks are widely separated and as we enter the II region the difference between two peaks diminishes and for III^{rd} region or for high chirality ρ_0 approaches value close to mean packing density. For larger activity $v_0 = 30$, in the first region ρ_0 remains close to 1 and the smoothly decay to moderate values in the II^{nd} region and finally approaches to 0.6 in the III^{rd} region. For large activities, we do not find bimodal distribution of $P(\rho_{loc})$ due to the very strong clustering in the system.

Now to further understand the effect of chirality on the structural ordering in the system we define the bond order parameter $\psi_6(t)$ [Lechner & Dellago (2008); Mermin (1968)].

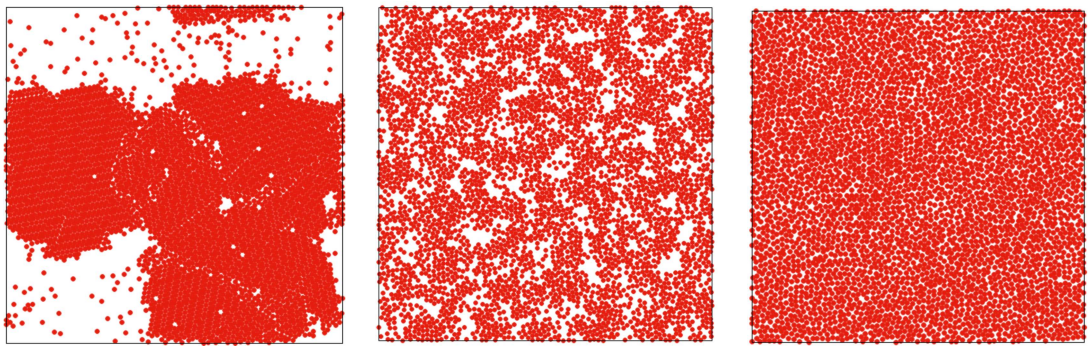

(a) (b) (c)

Fig. 4.4 Snapshot in three different region where $\psi(6)$ is around 0.55(a) for $\omega_0 = 0.001$, $\psi(6)$ is around 0.42 for $\omega_0 = 1.0$ (b), $\psi(6)$ is around 0.01 for $\omega_0 = 50$ (c) for $v_0 = 10$.

$\psi_6(t)$ is define by

$$\psi_6(t) = \frac{1}{N_p}\sum_{k=1}^{N_p}\sqrt{\frac{1}{N_k}\sum_{j=1}^{N_k} e^{i6\theta_{kj}}} \tag{4.7}$$

$\psi_6(t)$ measures the amount of hexagonal ordering in the system. For the perfect hexagonal close packed (HCP) structure, $\psi_6(t)$ will be close to 1 and for perfect random arrangement it is close to 0. In Fig. 4.5(b) we show the plot of mean value of $\psi_6(t)$, $\Psi_6(t) =< \psi_6(t) >$, where the mean $< .. >$ is average over time in the steady state and over

realisations. For small activity Ψ_6 remains close to small values 0.08 for small chirality and decay on increasing ω_0. For large activity and small chirality (region I), the $\Psi_6 \simeq 0.65$ and remains flat in the first region and then smoothly decay in region II and finally approaches very small values of the $\mathscr{O}(10^{-2})$ as system approaches III^{rd} region. Hence very clearly not only density shows the three types of clustering in three regions, but structural ordering also distinctly shows three regions with variation of chirality for high activities.

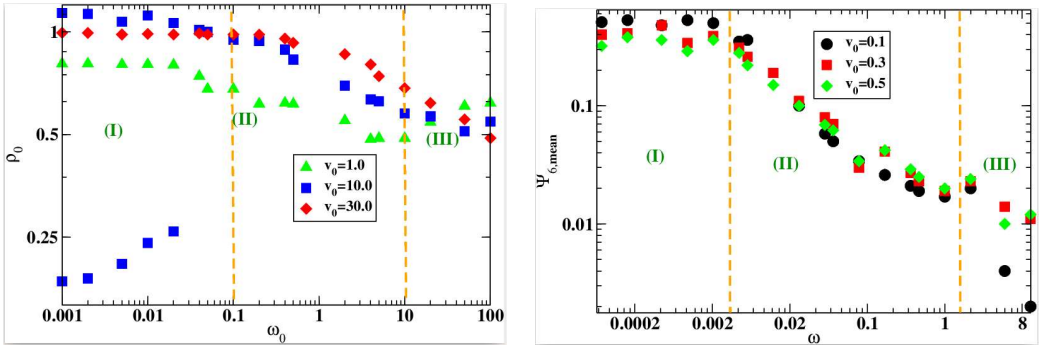

(a) (b)

Fig. 4.5 (a) ω_0 vs. peak value of histogram ρ_0 for different value of v_0(dotted orange line shows MAC,MIC and homogeneous phase marked with (I),(II),(III), (b) Plot of Mean value of ψ_6 vs. ω_0 for different value of v_0(dotted orange line shows MAC,MIC and homogeneous phase marked with (I),(II),(III)).

4.4 Phase Diagram

Based on the above results of Ψ_6 we have drawn the phase diagram in the plane of (v_0, ω_0). The system is found in three distinct phases: (i) (Homogeneous State (HS)) defined as small structural ordering $\Psi_6 < 0.025$, ρ_0 close to mean packing density 0.6, exponential CSD shown by triangles in the Fig. 4.6. This phase is found for large chirality and all activities. (ii) Microscopic cluster (MIC), defined as moderate structural ordering $0.025 < \Psi_6 < 0.25$, ρ_0 decays to moderate values and CSD shows the combination of exponential and power

law. This phase is shown as circles in the phase diagram. (iii) Macroscopic cluster (MAC), with large $\Psi_6 > 0.25$, large ρ_0 close to 1 and CSD decays as power law with power close to 2. This phase is shown using squares in the phase diagram. The color shows the value of Ψ_6 for different parameters (v_0, ω_0).

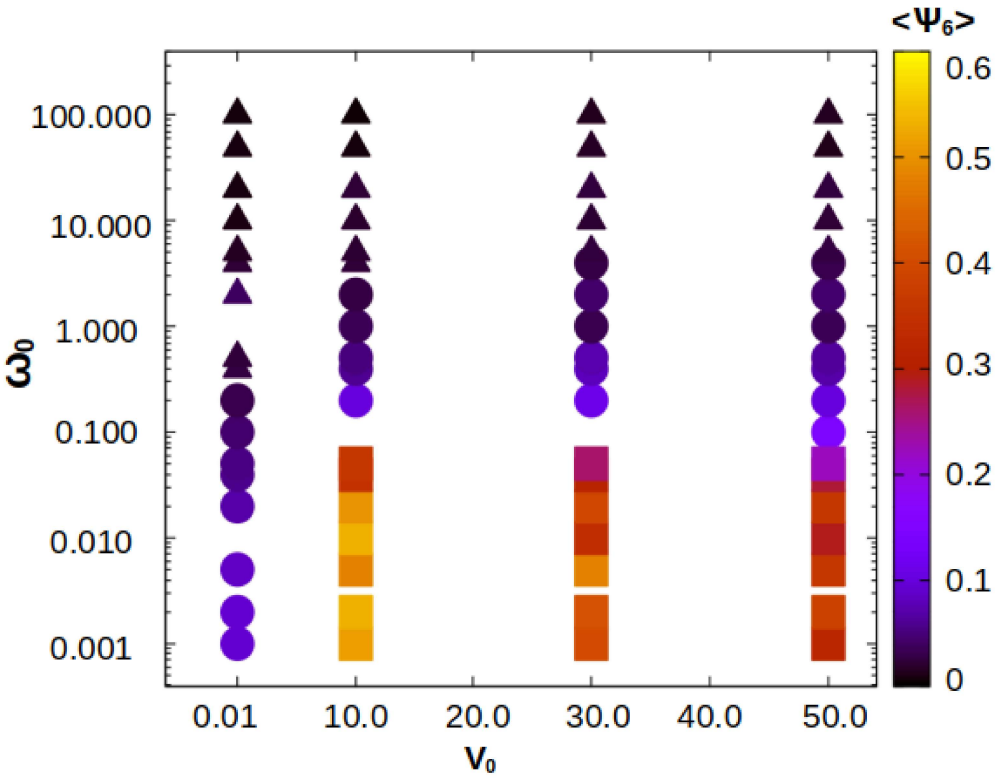

Fig. 4.6 (color online) Phase diagram of the system in $\omega 0$ vs. v_0 plane where square in MAC region, circle in MIC region, rectangle in homogeneous region (color intensity is for mean value of ψ_6.

4.5 Discussion

In conclusion we show the effect of varying the chirality on the collection of circle micro swimmer. The competition between activity and chirality leads to three distinct phases as

we slowly tune the chirality. For small chirality when linear motion dominates, effective dynamics of particles is enhanced, in comparison to single chiral particle with the same chirality. It leads to macroscopic clustering of particles. For intermediate chirality when linear and circle motion are comparable, the particles show weaker clustering with small cluster formation. The effective dynamics is suppressed. For strong circle swimmer of large chirality the motion of particle is mostly confined to its own location and no clustering is observed. The interaction among the particle leads to such three distinct phases, whereas for noninteracting chiral system only two types of dynamics is observed. The presence of three distinct phases for different chirality gives detail understanding of effect of chirality on the particles dynamics and steady state properties. This can be useful to use sorting of particles, based on their chirality. Hence our study can be useful in pharmaceutical industry as well as in clinical therapeutics and sorting of drugs [Abeylath & Turos (2008); Bechinger et al. (2016); Mijalkov & Volpe (2013); Nourhani et al. (2015)].

****